Autonomous screening of *C. elegans* identifies genes implicated in synaptogenesis

Matthew M Crane[1,5], Jeffrey N Stirman[1,2], Chan-Yen Ou[3], Peri T Kurshan[3], James M Rehg[4], Kang Shen[3] & Hang Lu[1,2]

Morphometric studies in multicellular organisms are generally performed manually because of the complexity of multidimensional features and lack of appropriate tools for handling these organisms. Here we present an integrated system that identifies and sorts *Caenorhabditis elegans* mutants with altered subcellular traits in real time without human intervention. We performed self-directed screens 100 times faster than manual screens and identified both genes and phenotypic classes involved in synapse formation.

Microscopy is a powerful tool widely used to investigate the biology of cells, tissues and organisms. Combining imaging with artificially induced perturbations (such as mutations, siRNA treatment or drugs) allows us to study the function of genes, RNAs and proteins and can serve to identify remedies for dysfunctions in these systems[1]. Recent technological developments have made automated microscopy and sample handling of single cells routine, allowing automated screens in cells to be performed[2]. This has enabled large-scale imaging and drug-screening studies in cultured cells[3–5]. Using statistical methods, researchers have developed high-content quantitative phenotypic descriptors of cells and used them to identify subtle phenotypes[5–7]. In contrast, automated screening of whole organisms through the use of a modified FACS system[8] or multiwell-plate methods has increased imaging and screening throughput, but these techniques have lagged behind in their capacity to identify subtle phenotypes of interest because of their relatively low resolution. A primary obstacle is that automated screening requires equipment that can robustly handle large sample numbers and a system for extracting and interpreting high-content imaging data. Recently, microfluidic approaches have enabled high-resolution imaging and screening throughput of *C. elegans*[9–11], but sorting has been based on user input[10] or simplistic criteria, such as the local image intensity[9].

Here we present a system for performing autonomous screens based on high-content quantitative morphometric features in *C. elegans*. The system combines a microfluidic device, computer-vision tools and a statistical framework to classify animals. The microfluidic device allows animals expressing a fluorescent reporter to be imaged and sorted rapidly (**Fig. 1a**). The acquired images are processed to identify the fluorescently labeled objects of interest using a two-stage computer-vision algorithm (**Fig. 1b–d**), and quantitative phenotypic descriptors are extracted and used to predict whether the animal has a pattern of interest (**Fig. 1e**,**f**). Finally, the microfluidic device sorts the identified mutants. Using this integrated system, we performed an autonomous forward screen in search of new classes of mutants affecting synaptogenesis.

The automated microfluidic system is optimized to simplify fabrication, minimize possible device failures such as clogging or delamination resulting from extended operation, and increase throughput while imaging at high magnification (**Fig. 1a** and **Supplementary Fig. 1**). It uses a simple 'load, image and sort' routine[9,10] that reliably manipulates animals and allows extended automated operation, even when dealing with animals that differ greatly in size, as is common after mutagenesis (**Supplementary Fig. 2**). When loaded, the animal is transiently (for ~10 s) cooled to ~3 °C. This rapidly immobilizes the animal for high-resolution image acquisition[9] without having to use feedback from the images to control mechanical immobilization mechanisms. The device used in this work is an optimized version of our previous device[9,10] that has been improved to allow fully automated operation. We have added to the system extensive external system-level components and error-handling capabilities to minimize the range of situations requiring human intervention (**Supplementary Note 1** and **Supplementary Fig. 3**). The optimizations in the screening protocol and the device allowed for a nearly fourfold increase (>220 animals per hour) in throughput relative to the first-generation system and enabled us to perform genome-wide forward genetic screens in a speedy manner (**Supplementary Note 1**).

To automate the morphometric criteria–based decision-making and sorting, we developed a computational framework that identifies specific fluorescently labeled objects of interest—such as the synapses or neuron soma—extracts quantitative phenotypic descriptors from these objects and classifies the animal on the basis of the descriptors (**Fig. 1b**,**c**). In contrast to the offline processing that most published computer-vision methods for biological analysis use[5,6,12], here real-time processing is critical to allow sorting decisions in forward genetic screens. We therefore designed the algorithm to balance two competing requirements: high

[1]Interdisciplinary Program in Bioengineering, Georgia Institute of Technology, Atlanta, Georgia, USA. [2]School of Chemical & Biomolecular Engineering, Georgia Institute of Technology, Atlanta, Georgia, USA. [3]Department of Biology, Howard Hughes Medical Institute, Stanford University, California, USA. [4]School of Interactive Computing, Georgia Institute of Technology, Atlanta, Georgia, USA. [5]Present address: SynthSys, University of Edinburgh, Edinburgh, UK. Correspondence should be addressed to H.L. (hang.lu@gatech.edu).

RECEIVED 6 JUNE; ACCEPTED 27 JULY; PUBLISHED ONLINE 19 AUGUST 2012; DOI:10.1038/NMETH.2141

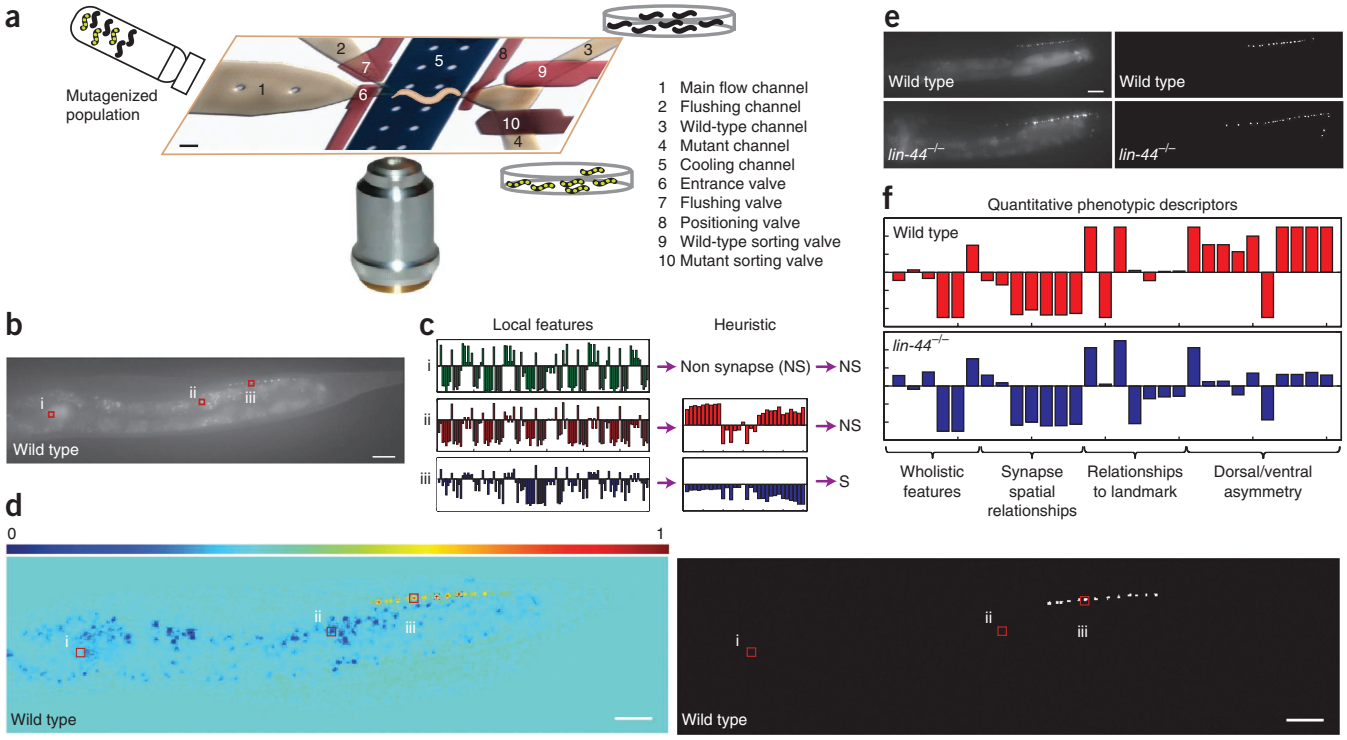

Figure 1 | Integrated system for autonomous screening of *C. elegans* expressing fluorescent reporters. (**a**) Schematic of the microfluidic device used to automate sample handling of a mutagenized *C. elegans* population that allows imaging and sorting. Scale bar, 150 µm. (**b**–**d**) Computer-vision framework used to identify the fluorescent reporter in a low signal-to-noise environment. Scale bars, 20 µm. (**b**) Maximum intensity–projection image of a representative wild-type animal acquired in the device; boxes show three distinct regions of the animal: (i) gut, (ii) fat granule and (iii) synapse. (**c**) Computer-vision framework applied to identify the objects of interest (synapses, S). For each pixel in **b**, local features are used to predict the probability that a pixel is a synapse; for points likely to be synapses, a second layer of information incorporating the spatial relationship between potential synapses is used to distinguish between gut or background autofluorescence and the fluorescent reporter of interest. (**d**) Left, a map of the image in **b** showing the probability that each point is a synapse; right, a thresholded image showing the identified synapses. (**e**,**f**) Statistical framework for quantitative phenotyping and autonomous decision-making during screening. (**e**) Representative images of wild-type animals and *lin-44*$^{-/-}$ mutants acquired in the device, and the resulting identified synapse locations. Scale bar, 20 µm. (**f**) Quantitative phenotypic descriptors extracted from the representative images. These descriptors are used to train the classifier for performing autonomous screens and predicting whether an animal is a mutant. The full list of the 30 descriptors can be found in **Supplementary Note 2**.

accuracy to maximize enrichment, which usually correlates with computational time, and minimal computational burden to maximize throughput (**Supplementary Note 2**).

We applied the method to identify an EGFP-tagged synaptic vesicle protein (RAB-3) in the DA9 motor neuron[13]. This is challenging because fluorescently labeled synapses are small, have limited numbers of fluorophores, and autofluorescent fat granules often have similar size and appearance to synapses (Online Methods). Automatically extracting quantitative phenotypic descriptors from these images requires the ability to distinguish relevant fluorescent structures from irrelevant ones. To identify synaptic mutants, one must be able to detect subtle changes in synapse location, size and fluorescent-marker intensity because synaptogenesis is a both complex and regulated process[13,14]. There is a low tolerance of false categorization of pixels belonging to synapses because a single synapse located far from stereotyped synapse positions could indicate an interesting mutant (**Supplementary Note 2**).

To minimize errors in identifying synapses, we designed the computer-vision framework to operate in two stages (**Fig. 1c**). First, the program identifies pixels associated with probable synapses using features based on the local neighborhood surrounding each pixel. Second, it uses these probable synapses to extract defining features on the basis of the relative positions of all the potential synapses in the image with respect to each other. The second-stage features were designed using a priori knowledge about patterns formed by synapses belonging to a single neuron, such as the fact that synapses are more likely to cluster near one another than to be randomly located in the worm body. Support vector machine classifiers were trained to evaluate these features and identify synapses (**Supplementary Notes 2** and **3** and **Supplementary Figs. 4**–**7**). This required manual annotation of images to identify the synapses and create a ground-truth library (**Supplementary Fig. 4**). The first-stage features were extracted from images within this library and, with the ground-truth labels, were used to train a classifier (**Supplementary Figs. 5** and **6**). This classifier was then used to identify probable synapses in images from the library; the second-stage features based on the positional relationships between probable synapses were extracted and used to train a second classifier (**Supplementary Fig. 7**). This framework was designed so that the identification took less time than the acquisition of the *z* stack (~4 s). The total processing time, including imaging and sorting, per imaged animal was ~10 s (**Supplementary Table 1**).

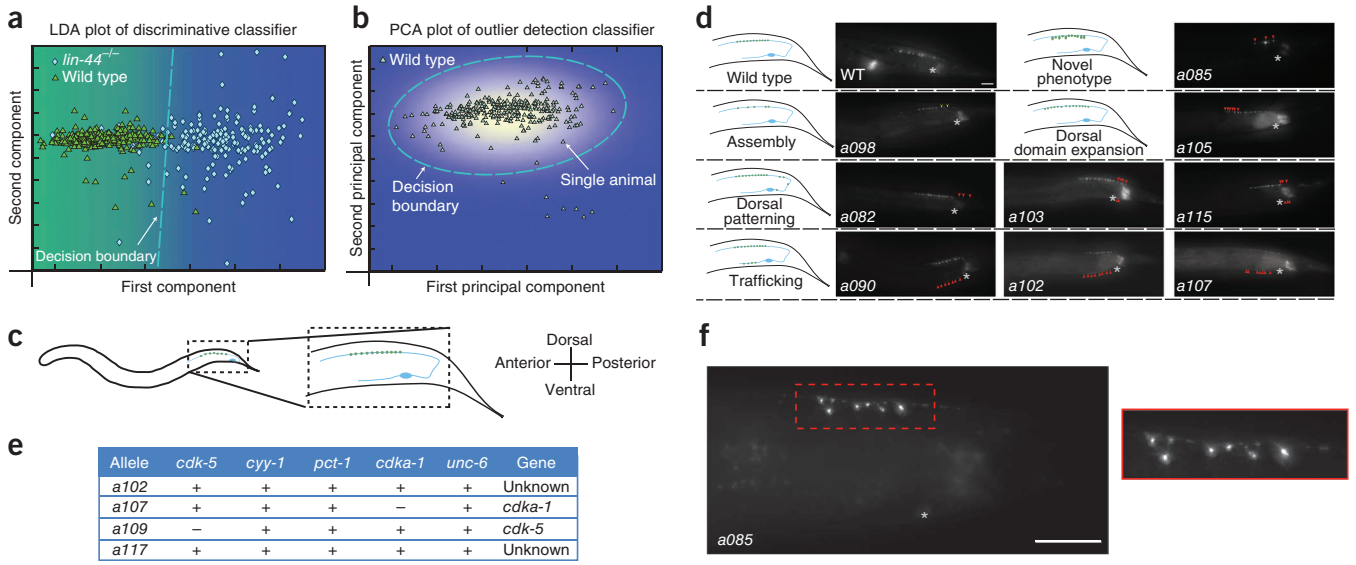

e

Allele	*cdk-5*	*cyy-1*	*pct-1*	*cdka-1*	*unc-6*	Gene
a102	+	+	+	+	+	Unknown
a107	+	+	+	–	+	*cdka-1*
a109	–	+	+	+	+	*cdk-5*
a117	+	+	+	+	+	Unknown

Figure 2 | Autonomous screens for *C. elegans* mutants with altered synaptic patterns. (**a**) Linear discriminant analysis projection of the phenotypic descriptors from wild-type and *lin-44*$^{-/-}$ animals used to train the discriminative classifier. Classification during screening was performed in the original high-dimensional space using a radial basis function–kernel support vector machine. A representative decision boundary is shown. (**b**) Principal-component analysis projection of the phenotypic descriptors from wild-type animals used for the outlier detection screen, showing a representative decision boundary. Classification during screening was performed in the original high-dimensional space. (**c**) Schematic location of the DA9 neuron (blue) within *C. elegans*, and its synapses (green). (**d**) Schematics of the phenotypic classes identified during autonomous screening, including both previously identified and novel phenotypic classes, are shown at left, with one or more representative images of alleles with phenotypes falling into the appropriate categories to the right. Asterisks, DA9 soma; red arrowheads, synapses in asynaptic regions; yellow arrowheads, gaps in synaptic regions. (**e**) Candidate mutants of a single phenocluster, trafficking, were selected for further investigation. Complementarity tests were performed between these new alleles and genes known to cause a similar dendritic puncta phenotype (*cdk-5* encodes a homolog of mammalian cyclin-dependent kinase 5; *cyy-1* encodes a cyclin Y homolog; *pct-1* encodes PCTAIRE class cell cycle kinase; *cdka-1* encodes a cyclin-dependent kinase 5–activating protein ortholog; *unc-6* encodes a netrin ortholog). Two alleles complemented genes known to act within this pathway (+), and two alleles failed to complement any of the known genes (–). (**f**) Images corresponding to the mutant *a085* phenotype, showing a novel pattern of enlarged spine-like protrusions. Scale bar, 20 µm; asterisk indicates DA9 soma.

This is a two-orders-of-magnitude savings in time compared to that required for a manual screening method that requires picking, mounting, imaging, manually quantifying phenotypic features using software such as ImageJ, and classifying and rescuing the animals (>20 min). The computer-vision framework exhibits an overall pixel accuracy of >99.9% when estimated by fivefold cross-validation (**Supplementary Fig. 8**). Once synapses are identified in each image, we use the overall synaptic pattern to extract 30 quantitative descriptors of the phenotypes such as the average size, shape, number and location of the synapses (**Fig. 1f** and **Supplementary Note 2**). These features are used to classify an animal as wild type or mutant with high accuracy and limited bias (**Supplementary Fig. 9**).

We used two types of classifiers to screen ethyl methanesulfonate–mutagenized EGFP::RAB-3–labeled worm populations and classify animals as wild type or mutant: a discriminative classifier and an outlier detection classifier (**Fig. 2a**,**b**). The discriminative screen used both wild-type animals and a known mutant (*lin-44*$^{-/-}$)[13], which has synapses present in a posterior asynaptic domain, to train the classifier and maximize the differences between the phenotypic descriptors of both populations. To train the classifier, ~130 wild-type animals and ~80 *lin-44*$^{-/-}$ mutants were imaged and quantitatively phenotyped using the system. Using two populations allowed the classifier to remove irrelevant descriptors that provide limited discriminative power. Because the classifier uses the known mutant to judge the performance of individual phenotypic descriptors, it can provide a reduced false positive rate, but at the potential cost of focusing the screen only on mutants with phenotypes similar to the known mutant (**Fig. 2a**). Although useful, this type of screen is less likely to find new classes of phenotypes. To screen more broadly and search for novel mutant classes, we used an outlier detection scheme; ~400 wild-type animals were imaged and used to model the wild-type population. The wild-type phenospace was modeled as a multivariate Gaussian, and mutagenized animals with a cumulative distribution function <0.1% of the wild-type phenospace were sorted as mutants (**Fig. 2b**). This allows screening for completely novel patterns, with the potential trade-off of a higher false positive rate.

To compare the discriminative powers of each screening method, and to obtain quantitative metrics on screening performance, we performed two small-scale screens. The discriminative classifier was used to screen ~1,000 haploid genomes, whereas a screen of ~1,500 haploid genomes was done with the outlier detection approach (**Supplementary Note 4**). Both screens resulted in comparable false positive (~70%) and false negative (~10%) rates (Online Methods), and this similarity was due to optimal setting of the decision boundary and selection of highly relevant phenotypic descriptors. Previous manual screens resulted in a discovery rate of about one mutant per few thousand haploid genomes. In contrast, our screens resulted in a discovery rate of one mutant per several hundred animals, and they included phenotypes similar to those previously published[13–15] as well as

novel ones. This higher discovery rate implies a potential ability to identify more genes affecting the phenotype of interest when compared with current methods.

To demonstrate our ability to perform large-scale experiments, we screened ~20,000 haploid genomes (Online Methods) and identified nearly 60 mutants with altered phenotypic features. The majority of this screening was performed with an outlier detection approach. From all screens, we obtained several phenotypic classes of mutants, and 24 animals were further characterized, including one mutant that exhibited a strikingly novel phenotype (**Fig. 2c**,**d** and **Supplementary Table 2**). Some of these mutants showed phenotypes similar to that of mutants with impaired cyclin-dependent kinase 5 pathway function[15]. Notably, complementation tests revealed two novel alleles (*a117*and *a102*) and two alleles of genes previously implicated in this pathway (*a107* and *a109*) (**Fig. 2e**). Allele *a085* has a morphological phenotype that has not been previously described in these types of screens: axons contain enlarged spine-like protrusions filled with synaptic markers (**Fig. 2f**). The allele is mapped to a small region on chromosome IV. This demonstrates that our system not only is capable of finding alleles of previously manually identified genes but also has the ability to identify novel genes and phenotypes missed by previous manual screens.

Our system is both camera and microscope independent, and it can be easily adapted in other laboratories and for other biological questions based on morphometric measures. As shown in this work, it allowed us to perform autonomous *C. elegans* screens searching for subtle subcellular changes using quantitative phenotypic descriptors. We screened at a sustained rate of over 100 haploid genomes per hour and identified a novel phenotype too subtle to be reliably identified by eye. Applied to additional forward-genetic, RNA interference or drug screens, this method not only will allow faster screens but also can help find more genes and interactions than previously possible.

METHODS

Methods and any associated references are available in the online version of the paper.

Note: Supplementary information is available in the online version of the paper.

ACKNOWLEDGMENTS

We thank funding from the US National Institutes of Health, US National Science Foundation, Alfred P. Sloan Foundation and Howard Hughes Medical Institute.

AUTHOR CONTRIBUTIONS

M.M.C. wrote the software, designed the microfluidic device and performed the screens. M.M.C. and J.N.S. designed and built the external system components. C.-Y.O. performed the complementation tests. P.T.K. performed the mapping and provided valuable reagents. M.M.C., J.N.S., J.M.R., K.S. and H.L. designed the experiments and prepared the manuscript.

COMPETING FINANCIAL INTERESTS

The authors declare no competing financial interests.

Published online at http://www.nature.com/doifinder/10.1038/nmeth.2141. Reprints and permissions information is available online at http://www.nature.com/reprints/index.html.

1. Jorgensen, E.M. & Mango, S.E. *Nat. Rev. Genet.* **3**, 356–369 (2002).
2. Huang, K. & Murphy, R.F. *BMC Bioinformatics* **5**, 78 (2004).
3. Whitehurst, A.W. *et al. Nature* **446**, 815–819 (2007).
4. Jones, T.R. *et al. Proc. Natl. Acad. Sci. USA* **106**, 1826–1831 (2009).
5. Collinet, C. *et al. Nature* **464**, 243–249 (2010).
6. Bakal, C., Aach, J., Church, G. & Perrimon, N. *Science* **316**, 1753–1756 (2007).
7. Perlman, Z.E. *et al. Science* **306**, 1194–1198 (2004).
8. Doitsidou, M., Flames, N., Lee, A.C., Boyanov, A. & Hobert, O. *Nat. Methods* **5**, 869–872 (2008).
9. Chung, K., Crane, M.M. & Lu, H. *Nat. Methods* **5**, 637–643 (2008).
10. Crane, M.M., Chung, K. & Lu, H. *Lab Chip* **9**, 38–40 (2009).
11. Rohde, C.B., Zeng, F., Gonzalez-Rubio, R., Angel, M. & Yanik, M.F. *Proc. Natl. Acad. Sci. USA* **104**, 13891–13895 (2007).
12. Murray, J.I. *et al. Nat. Methods* **5**, 703–709 (2008).
13. Klassen, M.P. & Shen, K. *Cell* **130**, 704–716 (2007).
14. Poon, V.Y., Klassen, M.P. & Shen, K. *Nature* **455**, 669–673 (2008).
15. Ou, C.-Y. *et al. Cell* **141**, 846–858 (2010).

ONLINE METHODS

***C. elegans* culture**. Worms were cultured according to established methods[16]. Mutagenesis was performed on age-synchronized L4 animals using ethyl methanesulfonate (EMS) according to standard protocols[17]. The overall scheme is shown in **Supplementary Figure 1**. Briefly, when the animals reached the L4 stage, a large number of synchronized wild-type animals carrying the *wyIs85* transgene were suspended in a buffer solution and 20 mM EMS (Sigma-Aldrich) for a period of 4 h. After the incubation, the animals were rinsed with M9 buffer solution and placed on plates. These P_0 animals were allowed to grow to adults, and once the F_1 progeny from these animals became adults, the F_2 offspring were age synchronized. F_2 embryos were obtained by bleaching F_1 adults using a solution containing about 1% NaOCl and 0.1 M NaOH, washing them in M9 buffer and culturing them for 24 h. Animals were then transferred and cultured on nematode growth medium (NGM) plates seeded with *Escherichia coli* OP50 until L4 stage. The strains used in this project included XA7810: N2, *wyIs85* (Pitr-1 *pB::gfp::rab-3*); XA7812: *lin-44(n1792)I* and *wyIs85*(Pitr-1 *pB::gfp::rab-3*).

For imaging and screening, animals were washed and suspended in M9 solution containing 0.01% (v/v) Triton X-100 (Sigma-Aldrich). This prevented the animals from adhering to the tubing during injection. After we washed the animals off the plates, the animals were allowed to settle, the supernatant was removed and additional M9 was added. Animals were screened under a compound microscope using a 40× (NA = 1.4) oil objective using the microfluidic chips. Sorting decisions were made based on differences in the reporter expression pattern or intensity; animals of potential interest were sorted into the mutant outlet and were collected directly from tubing connected to the mutant outlet with M9 solution containing 0.01% Triton X-100. Animals were subsequently transferred to individual plates for culture and further examination. SNIP-SNP mapping and complementation tests were performed using standard protocols.

Materials and equipment. The equipment used during our experiments includes the following: a Peltier cooler (PJT-5 30-mm^2 and PJT-6 40-mm^2 Peltier coolers); a copper heat exchanger (custom designed and machined); a peristaltic pump for coolant, 400 F/A (Watson Marlow); a digital I/O card (Pacdrive from Ultimarc); solenoid valves and manifold (3-way 10-mm solenoid valve, 188 series, ASCO valve); a microscope (Leica DM4500) with lens (63× oil, NA = 1.4); and a camera (Infinity 3-1, Lumenera).

Automation, handling of multicellular organisms and system design. The software we used during screening is provided online to accompany this paper (**Supplementary Software**). Because of differences in equipment, this software is primarily intended as a guide for development of customized code for the end user. The code contains functions used to operate the microfluidic device and functions to extract relevant information from the fluorescent images. The optimized feature extraction and phenotypic parameters can be modified to focus on identification of other small, fluorescent objects. More information can be found in a 'readme' file available with the software.

The completed microfluidic device is shown in **Supplementary Figure 2a**. The device is a standard two-layer PDMS instrument[18,19], similar to devices used in our previous work[9,10,20], fabricated using a rapid prototyping method and thermal bonding between layers (**Supplementary Fig. 2b**). Rather than using conventional full-closure valves that rely on a curved cross-section of the flow layer, this device uses a rectangular flow layer. Although valves incapable of fully closing are typically considered drawbacks in microfluidic devices, in this case they could be used advantageously to simplify the design. Because the valves always allow a small amount of flow (**Supplementary Fig. 2c**), the device was designed using partial closure valves to position animals in the imaging channels instead of using suction channels[9].

In addition to the development of a microfluidic device for screening, external systemic components were required to allow for automated sorting. This required a closed-loop control system and the development of specific hardware to interface with and control the on-chip components. Creating external components that would allow computerized control of on-chip components was necessary (**Supplementary Fig. 1**).

Because we needed to run the system for a long period during the screen, a comprehensive framework was developed for handling errors robustly (**Supplementary Fig. 3**). This includes integrating an external macroscale control component with the microfluidic device to allow closed-loop control, error handling routines to reduce the need for operator intervention for the closed-loop control and optimization of the operational sequence to minimize the amount of time spent per animal. The entire system was coded in MATLAB. External calls were made to the machine learning libraries and a .dll file for valve control operation. Because of potential stability issues with MATLAB operation, however, it could be advisable for future efforts to focus on the open microscopy environment and code in a more robust language such as Java.

Genetic screening. The screening methodology was optimized to maximize the number of independent F_2 animals screened and to minimize the likelihood of screening clonal siblings. This was done by pooling F_2 animals from ~1,500 F_1 mothers and then screening a subset of this group. Because of the screening methodology, the number of haploid genomes cannot be directly calculated, but several assumptions have to be made regarding the sampling from the F_2 populations. These assumptions are derived from an earlier paper[21].

After mutagenesis, P_0 animals were placed on large NGM plates, ~25 animals per each of ten plates. Each P_0 animal has around 60 progeny. This results in approximately 1,500 F_1 animals per plate, or 3,000 haploid genomes. Given that F_1 animals are A/B, we can assume that half of the animals are homozygous (A/A or B/B), and the naive assumption is that for every two F_2 animals screened, we have screened one haploid genome. On average, 500 F_2 animals were screened from each of these populations, which resulted in 250 haploid genomes. Given that we were sampling from a larger population of animals, there is the possibility that an F_2 animal could be homozygous for the same genome present in an animal that was previously screened. The probability of this occurring was calculated as $1 - (2{,}999/3{,}000)^{250} = 0.08$. Given there were 3,000 haploid genomes present, we screened $0.08 \times 3{,}000 = 240$. This yields a ratio of 240/500 = 0.48, implying that because we have screened a total of ~40,000 animals, that corresponds to nearly 20,000 haploid genomes.

Following screening, the animals identified were cloned and then verified by reimaging. Once the identified mutants have been cloned and decontaminated, it is necessary to verify that the animals are probable mutants. Furthermore, because genetic validation by sequencing is such a slow and time-consuming process, it is important to visually confirm that each of the animals to be mapped or sequenced indeed has an altered synaptic expression. Validation was done with standard worm protocols using a worm-slide and sodium azide for immobilization. A small population (~15–20) of animals of each genotype was imaged, and these images were used to determine whether the animals were actual mutants, and thus the accuracy of the screening. Some of the mutants were phenotyped with larger numbers and were characterized in greater detail to predict the potential pathway that was affected (**Supplementary Table 2**). Each of the genotypes classified as mutants of interest was phenotyped. For the purpose of these results, animals that were sorted as mutants but failed to produce any offspring that could be used to verify whether they had been correctly or incorrectly sorted were removed from the results.

To evaluate the accuracy of the screening protocol, images of all processed animals were collected and analyzed to determine whether animals were correctly or incorrectly sorted as wild-type animals. The false negative rate, which we calculated by comparing the manual scores to the computer scores, was used to determine the accuracy of the algorithm. The screen using the discriminative classifier resulted in a false positive rate of 69%, a false negative rate of 9% and a theoretical enrichment of 6,000%. The screen using the outlier detection approach resulted in a false positive rate of 74%, a false negative rate of 7% and an enrichment of 6,000%. The marginally higher false negative rate could be a result of the discriminative classifier not recognizing some mutant phenotypes, or merely the sample size. The false positive rates of these classifiers are similar to or better than the manual methods because of animal-to-animal variations and the manual method's subjectivity in scoring the phenotypes. These false positive animals also do not pose an issue in these rare-sort problems because it is a small number of candidate mutants that need to be characterized in the following steps.

False positives were calculated using the following equation in which sterile animals were removed from the denominator:

$$\mathrm{FP} = \frac{\text{Wild type sorted as mutants}}{\text{Animals sorted as mutants}}$$

The false negative rate was calculated using the following equation:

$$\mathrm{FN} = \frac{\text{Mutants sorted as wild type}}{\text{Mutants sorted as mutants} + \text{Mutants sorted as wild type}}$$

The upper bound of the enrichment was calculated using the equation

$$\text{Enrichment} = \frac{\left(\dfrac{\text{Mutants correctly sorted}}{\text{Number of animals sorted as mutants}}\right)}{\left(\dfrac{\text{Mutants in starting population}}{\text{Animals in starting population}}\right)}$$

16. Brenner, S. *Genetics* **77**, 71–94 (1974).
17. Wood, W.B. *The Nematode Caenorhabditis elegans* (Cold Spring Harbor Laboratory Press, 1988).
18. Unger, M.A., Chou, H.P., Thorsen, T., Scherer, A. & Quake, S.R. *Science* **288**, 113–116 (2000).
19. Duffy, D.C., McDonald, J.C., Schueller, O.J.A. & Whitesides, G.M. *Anal. Chem.* **70**, 4974–4984 (1998).
20. Chung, K. & Lu, H. *Lab Chip* **9**, 2764–2766 (2009).
21. Ellis, R.E., Jacobson, D.M. & Horvitz, H.R. *Genetics* **129**, 79–94 (1991).

doi:10.1038/nmeth.2141